Possible topological superconductivity in the topological crystalline insulator $(Pb_{1-x}Sn_x)_{1-y}In_yTe$

I. Pletikosić,[1,2] T. Yilmaz,[3] B. Sinkovic,[4] A. P. Weber,[3,5] G. D. Gu,[1] and T. Valla[1,6,*]

[1]*Condensed Matter Physics and Materials Science Department, Brookhaven National Laboratory, Upton, New York 11973, USA*

[2]*Department of Physics, Princeton University, Princeton, New Jersey 08544, USA*

[3]*National Synchrotron Light Source, Brookhaven National Laboratory, Upton, New York 11973, USA*

[4]*Department of Physics, University of Connecticut, Storrs, Connecticut 06269, USA*

[5]*ICFO-Institut de Ciencies Fotoniques, The Barcelona Institute of Science and Technology, 08860 Castelldefels, Barcelona, Spain*

[6]*Donostia International Physics Center, 20018 Donostia-San Sebastian, Spain*

(Received 13 September 2023; revised 6 November 2023; accepted 16 November 2023; published 30 November 2023)

Superconductivity in topological insulators is expected to show very unconventional features such as a $p + ip$ order parameter, Majorana fermions, etc. However, intrinsic superconductivity has been observed in a very limited number of materials in which the pairing symmetry is still a matter of debate. Here, we study the topological crystalline insulator (TCI) $(Pb_{1-x}Sn_x)_{1-y}In_yTe$, for which a peculiar insulator to superconductor transition was previously reported near the gap inversion transition, where the system is nearly a three-dimensional Dirac semimetal. Both the existence of superconductivity near the three-dimensional Dirac semimetal and the occurrence of an insulator to superconductor transition in an isotropic material are highly unusual. We suggest that the observed phenomena are related to the intrinsic instability of a three-dimensional Dirac semimetal state in $(Pb_{1-x}Sn_x)_{1-y}In_yTe$ and "flattening" of the bulk valence and conduction bands as they acquire a Mexican-hat-like dispersion on the inverted side of the phase diagram. This favors the pairing instability if the chemical potential is pinned to these flat regions.

DOI: 10.1103/PhysRevB.108.205157

I. INTRODUCTION

A three-dimensional (3D) Dirac point with linear dispersion in all three directions can be created at a time-reversal-invariant momentum by tuning an external parameter m if the valence and conduction bands have opposite parities [1–3]. This occurs, for example, at a quantum critical point ($m = m_c$) between a normal insulator and a Z_2 topological insulator or a topological crystalline insulator. In the gap-inverted (topological) phase, the topological states that unavoidably exist at boundaries [4,5] have been the focus of both theoretical and experimental studies over the last ∼2 decades [6–19]. The approach to the 3D Dirac quantum critical point requires fine tuning of an external parameter m such as pressure or a material composition that drives the transition [20,21]. In general, a 3D Dirac point with fourfold degeneracy does not have a topological number, and it is therefore unstable against small perturbations. However, it was later realized that particular lattice symmetries may result in a band structure with stable 3D Dirac cones, and shortly after the theoretical prediction [22,23], several materials, including Na_3Bi and Cd_3As_2, were experimentally identified as 3D Dirac semimetals (DSMs) [24–26]. While the 3D Dirac points in these 3D DSMs are protected by crystal symmetries, the generally unprotected 3D Dirac points at the band inversion transitions could potentially display a very rich physics. A particularly interesting example is In-doped $Pb_{1-x}Sn_xTe$, a topological crystalline insulator (TCI), which shows an intriguing transition from a relatively good insulator to a robust superconductor as a function of In concentration when in the vicinity of a transition between a trivial and topological crystalline insulator at $x = x_c \approx 0.36$ [27–32]. The insulator to superconductor transitions have usually been observed in thin films and in some quasi-2D materials as a consequence of strong quantum phase fluctuations due to reduced dimensionality [33,34]. In a relatively isotropic 3D material, such a transition is highly unexpected. The appearance of superconductivity itself is also highly unusual in a system in which the low-energy quasiparticles resemble 3D Dirac fermions with a linearly vanishing density of states.

Another interesting aspect of In-doped $Pb_{1-x}Sn_xTe$ is the possibility that its superconducting phase represents an intrinsic topological superconductor [35]. Although for a long time the focus has been on Sr_2RuO_4, which is considered to be an intrinsic chiral p-wave triplet superconductor [36–38], more recent results excluded that possibility [39]. Currently, the number of bulk topological superconductors is very limited, with $Cu_xBi_2Se_3$ and $Sn_{(1-x)}In_xTe$ being the rare candidates, with T_c around 2–4 K [40–42]. $Cu_xBi_2Se_3$ is found to be very inhomogeneous, with a small superconducting volume, and therefore is not ideal for spectroscopic studies that could determine the order parameter or the existence of Majorana fermions. In more homogeneous $Sn_{(1-x)}In_xTe$, spectroscopic studies have provided evidence for the odd-parity pairing and topological superconductivity [42]. More recently, several candidates for topological superconductors were discovered in materials that make natural superlattices involving rocksalt $Pb_{1-x}Sn_xTe$ layers, in which the specific heat suggests the existence of gap nodes [43,44].

*tonica.valla@dipc.org

An alternative avenue towards topological superconductivity in heterostructures involving superconductors and topological insulators has been also explored [35,45,46], including TI films on cuprate high-temperature superconductors (HTSCs). However, studies claiming a large superconducting gap on the topological surface state on Bi_2Se_3 grown on Bi2212 [47,48] were later shown to be incorrect [49]. The complete absence of the proximity effect seems to be intrinsic to HTSCs; films grown on cuprate superconductors donate electrons, thus making the interface so underdoped that superconductivity completely vanishes [50,51], making HTSCs inadequate for inducing topological superconductivity.

Here, we show that the topological crystalline insulator $Pb_{1-x}Sn_xTe$ might be a good candidate for an intrinsic topological superconductor when doped with indium. When near the gap inversion point, In-doped $Pb_{1-x}Sn_xTe$ shows a transition between a real bulk TCI and a bulk superconductor [31]. By studying the details of electronic structure using angle-resolved photoemission spectroscopy (ARPES), we suggest that this peculiar transition is caused by the transformation of bulk bands from the linear, 3D-Dirac-like to "Mexican-hat-like" ones on the topological side, where an inevitable flattening at the onset of that transformation must occur. This transformation could support superconductivity when the flat regions are brought near the chemical potential via In doping.

II. EXPERIMENTAL DETAILS

The ARPES experiments were carried out on a Scienta SES-R4000 electron spectrometer at beamline U5UA at the National Synchrotron Light Source (NSLS) in the photon energy range from 12.5 to 62 eV and at the OASIS Laboratory at Brookhaven National Laboratory, using monochromatized He $I\alpha$ radiation [52]. The core level spectra were taken at NSLS using 110–150 eV photons. The total instrumental energy resolution was ∼6 meV at 12–24 eV, ∼12 meV at 50–62 eV, and ∼30 meV at 110–150 eV photon energy. Angular resolution was better than ∼0.15° and 0.4° along and perpendicular to the slit of the analyzer, respectively.

Thick, bulklike (2–5 μm) films of (111) $(Pb_{1-x}Sn_x)_{1-y}In_yTe$ were grown on either BaF_2 or Bi_2Te_3 substrates, using the open hot wall epitaxy method [53] and a single-source evaporator loaded with crushed single crystals of $(Pb_{1-x}Sn_x)_{1-y}In_yTe$ [29]. The BaF_2 substrates were cleaved in air and annealed in ultrahigh vacuum (UHV) at 600 °C for 1 h, while the Bi_2Te_3 substrates were cleaved in UHV before film deposition. During growth, the substrate was kept at ∼300 °C. The thickness was determined by the quartz crystal thickness monitor. Composition of the films was checked by measuring the photoemission from the shallow core levels (In 4*d*, Sn 4*d*, Te 4*d*, and Pb 5*d*) and comparing them with the spectra of the source material that was broken *in situ*. After ARPES experiments, films were checked for superconductivity by superconducting quantum interference device magnetometry. In several cases, T_c in the film was slightly higher than in the source material, with a maximum T_c of ∼6 K.

III. PURE $Pb_{1-x}Sn_xTe$

Figure 1 shows the ARPES data from the film on the trivial side of the phase diagram: $Pb_{0.85}Sn_{0.15}Te$. The (111) surfaces can be either Te- or Pb-Sn-terminated, and in Pb-rich films ($x < 0.3$), both terminations can be distinguished in ARPES, as shown in Fig. 1. Figures 1(a)–1(c) represent the in-plane electronic structure of the mostly Te-terminated surface, while Figs. 1(d) and 1(e) represent mostly Pb-Sn termination. The two terminations can be distinguished because they display slightly different ratios between the Te 4*d* and Pb 5*d* (Sn 4*d*) core levels. Both terminations show almost identical (aside from the ∼0.2 eV energy shift) and fairly isotropic in-plane dispersion. Both also display bands split in a Rashba-like manner, near their extrema. The splitting is more obvious on the Te-terminated surface, indicating a stronger inversion symmetry breaking surface field that would result in larger spin-orbit interaction. However, the bands disperse rather strongly with k_z [Figs. 1(g) and 1(i)], and it is not clear whether the Rashba-like split features are the surface states. Indeed, a suggestion that the bulk bands could also display Rashba splitting with the breaking of the inversion symmetry because the surface goes deep enough into the crystal was recently discussed in relation to a new candidate for a spin-triplet superconductor, UTe_2 [54,55]. Here, we note that the momentum width of the valence band along k_z ($\Delta k_\perp \sim 0.06$ Å^{-1}) is comparable to the in-plane width, implying a surprisingly large ARPES probing depth at these photon energies. The more conventional possibility is that the observed Rashba-like split features are trivial precursors of the topological surface states. Their apparent dispersion with k_z, or, alternatively, their existence only inside an extremely limited k_z interval corresponding to the very vicinity of the *L* point of the Brillouin zone (BZ), would suggest their strong mixing with the bulk states. Similar effects were observed on the topological side of $Pb_{1-x}Sn_xSe$ [56].

On the surface terminated mostly by Pb-Sn, the bottom of the bulk conduction band is visible at $\hbar\nu = 17$ eV, enabling the determination of the direct band gap $\Delta_L \approx 130$ meV at 50 K, in agreement with early optical studies at similar compositions [57,58]. The photon energy dependence that gives access to the out-of-plane electronic structure is shown in Figs. 1(g) and 1(i) for the mostly Te-terminated surface. The set of $k_y = 0$ spectra measured at photon energies ranging from 12.5 to 23 eV is converted to k_z using the free electron approximation for the final photoemission state, with $V_0 = 13$ eV for the "inner" potential. The emission at $\hbar\nu = 17$ eV corresponds to $k_z = 2.6$ Å, the *L* point between the second and third bulk Brillouin zones (BBZs). The constant-energy contours, shown for the Te-terminated surface [in-plane, Fig. 1(b); out-of-plane, Fig. 1(g)] correspond to $E = -60$ meV as there is no intensity at the Fermi level. The contour is elongated in the k_z direction, in agreement with the band structure calculations [20]. It also shows a limited span of the Rashba-like features in this direction. The in-plane dispersion [Fig. 1(h)] is approximately 2–3 times faster than the out-of-plane one [Fig. 1(i)], and aside from an ∼130 meV gap, the electronic structure already seems very close to the 3D DSM.

Figure 2 shows the 3D electronic structure of a film on the TCI side, but very near the inversion transition: $Pb_{0.6}Sn_{0.4}Te$. At this composition, we no longer observe either Rashba-like split states or two distinct terminations. The reason is probably the fact that with increasing *x*, the samples become

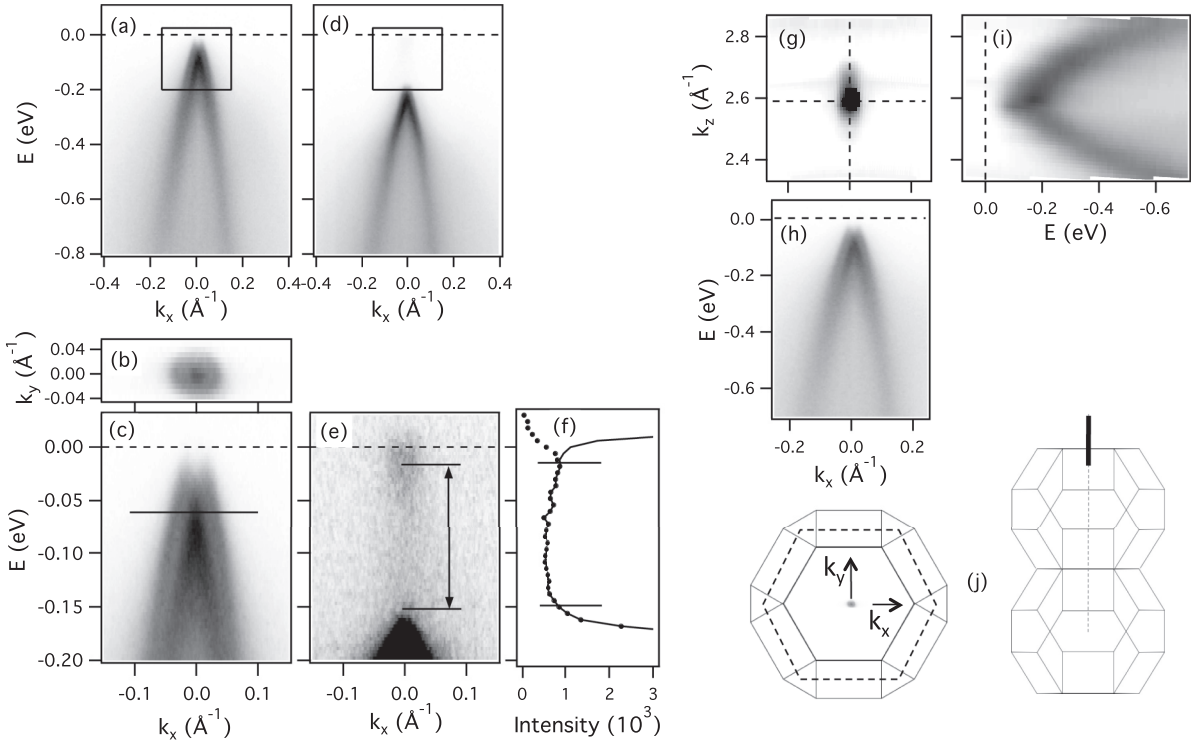

FIG. 1. Electronic structure of a thick (111) $Pb_{0.85}Sn_{0.15}Te$ film. (a) Valence band dispersion along the $\bar{\Gamma}$-$\bar{K}$ momentum line of the surface Brillouin zone (SBZ) for the Te-terminated surface. (b) Constant-energy contour of the ARPES intensity at $E = -60$ meV [marked in (c) by the solid line] as a function of the in-plane momentum. (c) Close-up of the spectral region marked by the rectangle in (a). (d) and (e) show the corresponding spectra for the Pb-Sn-terminated surface. (f) Energy distribution curve at $k_x = 0$ from (e). The raw intensity and that divided by the Fermi distribution are plotted as dots and the solid line, respectively. The spectra in (a)–(f) were recorded at $\hbar\nu = 17$ eV, corresponding to $k_z = 2.6$ Å (L point in between the second and third bulk BZs). The arrow in (e) represents the gap between the VB and CB, $\Delta_L \approx 130$ meV. (g) ARPES intensity for the Te-terminated surface at $E = -60$ meV as a function of k_z along the Γ-L-Γ line of the BBZ and k_x along the $\bar{\Gamma}\bar{K}$ line of the SBZ. (h) In-plane dispersion at $k_z = 2.6$ Å [same as (a)]. (i) k_z dispersion of the valence band along the Γ-L-Γ line of the bulk BZ. Intensity maps in (g) and (i) were produced from spectra taken at photon energies ranging from $\hbar\nu = 12.5$ eV to $\hbar\nu = 24$ eV. All the spectra were taken at ∼50 K. (j) Projection of the bulk BZ to the (111) surface and the SBZ (dashed hexagon; left). The small circle at $\bar{\Gamma}$ is the same contour as in (b). The first and second bulk BZs with the probed region of k_z marked by a thick line.

significantly more hole doped, and for $x \geqslant 0.4$, we observe only hole pockets with very consistent sizes. The higher carrier concentration provides more effective screening of the surface potential, reducing the surface band bending. Consequently, the differences for different terminations should diminish. The Fermi surface [Fig. 2(a)] is a small ellipsoidal hole pocket, with an ∼3:1 ratio in k_z over the in-plane size. If the pocket is the bulk feature, as the strong k_z dispersion [Fig. 2(b)] indicates, and assuming an ellipsoidal shape, we can estimate the bulk carrier concentration to be $n_h \sim 1.2 \times 10^{18}$ cm^{-3} (four L pockets in the BBZ containing 3×10^{17} cm^{-3} holes each). The Fermi velocities, deduced from momentum distribution curve fitting, are 4.4 and 1.7 eV Å for the in- and out-of-plane directions, respectively. The topological surface state (TSS) probably overlaps with these (bulk) states, as was shown in n-type surfaces of $Pb_{1-x}Sn_xSe$ [18,19,59].

At higher energies, the contours become distorted and strongly trigonally warped, both below and above the L point [Fig. 2(f)], with the direction of warping being opposite across the zone boundary. This was predicted in the band structure calculations but never observed experimentally [20]. It seems from the spectra in Fig. 2 that this composition is, indeed, very close to the critical one at which the band inversion occurs. The bands are nearly linear, and the Fermi surface is very small. Unfortunately, as the films at this composition are always p type, we do not have access to the conduction band at low temperature. However, at room temperature, we could access it, and the spectrum [Fig. 2(d)] indicates that the gap is. indeed. negligible.

IV. EFFECTS OF INDIUM DOPING

Figure 3 shows the ARPES results for the trivial side of the $(Pb_{0.7}Sn_{0.3})_{1-y}In_yTe$ phase diagram, $x = 0.3$, with two different In concentrations, $y = 0$ and $y = 0.16$. The valence band in Figs. 3(c) and 3(d) again displays two states split in k in a Rashba-like manner. If, as previously discussed, these are the surface states peaking in intensity at the L point of the bulk BZ, they would indicate that the material is still on the trivial side of the phase diagram, and although they might make a significant contribution to the transport of thin samples [30], they are not protected by any topological invariance. In that sense, they are very similar to the conventional Rashba

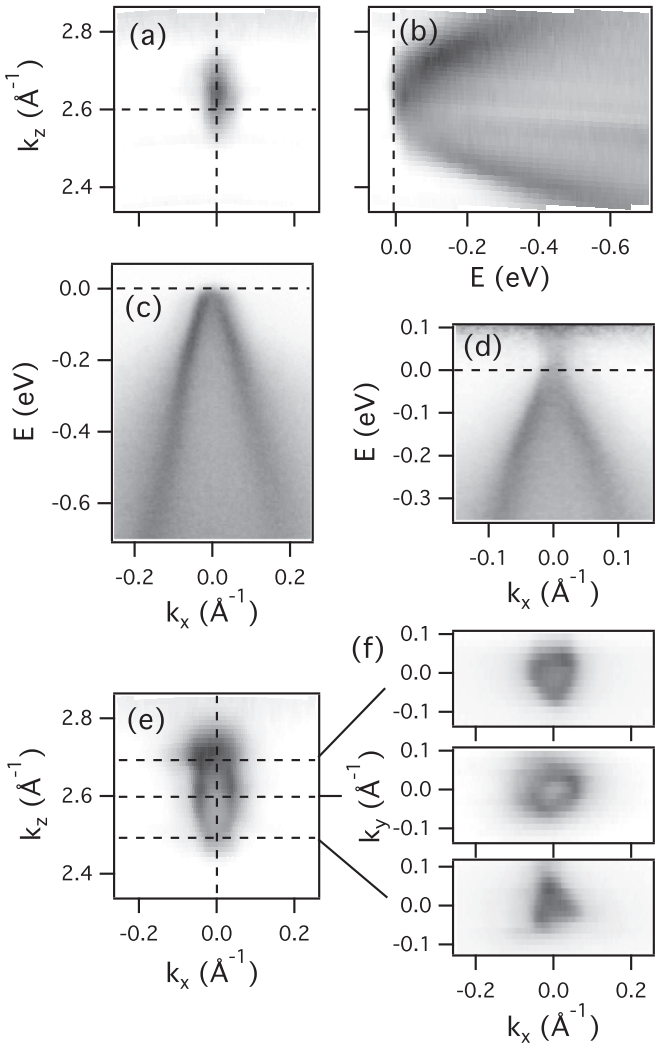

FIG. 2. Three-dimensional electronic structure of a thick (111) $Pb_{0.6}Sn_{0.4}Te$ film. (a) ARPES intensity at the Fermi level (Fermi surface) as a function of k_z along the Γ-*L*-Γ line of the BBZ and k_x along the $\bar{\Gamma}\bar{K}$ line of the SBZ. (b) k_z dispersion of the valence band along the Γ-*L*-Γ line, near the *L* point between the second and third BBZs. (c) Dispersion of the valence band along the $\bar{\Gamma}\bar{K}$ line of the SBZ, taken at 17 eV photon energy (corresponding to the *W*-*L*-*W* line in the bulk BZ). (d) The same as in (c), but recorded at ∼300 K and divided by the corresponding Fermi distribution. (e) Constant-energy contour at $E = -100$ meV as a function of k_x and k_z ($k_y = 0$). (f) Constant-energy contours of in-plane ARPES intensity at $E = -100$ meV, taken at $\hbar\nu = 15$ eV (bottom), $\hbar\nu = 17$ eV (middle), and $\hbar\nu = 19$ eV (top), corresponding to three different k_z, as indicated by dashed lines in (e). All the spectra were taken at 80 K, except for the spectrum in (d).

surface states on Au(111). Increasing the In concentration to $y = 0.16$ in Fig. 3(b) clearly shifts the Fermi level towards the bulk conduction band, and now the Rashba-like surface states can be seen on both the conduction side and the valence side, forming a double-cone-like shape, with a small gap still present between the two sides. This shows that at this composition, the material is very close to the critical point, at which the two cones should collapse into a single, ungapped one—and the topological surface states should be fully formed. A previous ARPES study provided evidence for topological surface states at $x = 0.4$ (without In) [15]. The crucial point here is that $(Pb_{0.7}Sn_{0.3})_{1-y}In_yTe$ does not become superconducting for any amount of In doping [27,30,31] up to the In solubility limit. On the contrary, initially metallic, $Pb_{0.7}Sn_{0.3}Te$ becomes a bulk insulator with In doping. However, at low temperature, the resistivity becomes dominated by the contribution from the surface states and saturates in thin samples [30,31], a clear sign that even the trivial surface states can significantly participate in transport in certain cases.

Figure 4 shows the effects of In doping on the electronic properties of $Pb_{0.5}Sn_{0.5}Te$, on the gap-inverted TCI side of the phase diagram. Without In, ARPES indicates a heavily hole-doped system with carrier concentration $n_h \sim 5 \times 10^{19}$ cm^{-3} (4 times 1.25×10^{19} cm^{-3}), almost two orders of magnitude larger than in the $Pb_{0.6}Sn_{0.4}Te$ sample. In-plane Fermi velocities show significant anisotropy, ranging from ∼2.2 to ∼6 eV Å. The slower states are likely bulk, while the fast dispersing ones are the TSS, as their velocity is similar to those spanning the gap in the In-doped case in Figs. 4(g) and 4(h). The out-of-plane Fermi velocity is ∼2 eVÅ. When doped with In, n_h dramatically decreases, and for $(Pb_{0.5}Sn_{0.5})_{0.7}In_{0.3}Te$, the chemical potential is shifted by ∼200 meV, from inside of the valence band to near the bottom of the conduction band (note that for this composition without indium, the inverted gap would be around 100 meV [60]). This shift in chemical potential seems to be in nice agreement with transport in $(Pb_{0.5}Sn_{0.5})_{1-y}In_yTe$, which displays rather interesting behavior: initially metallic ($y = 0$), the material becomes less conductive and shows an insulating bulk conductance at low In concentration ($y \approx 0.06$). However, at even higher In concentrations ($y \geqslant 0.1$), the material becomes metallic again, this time with the superconducting ground state [29,31]. This nonmonotonic behavior, together with our spectroscopic results, suggests that the carriers, initially holes, turn into electrons with sufficient In doping. This is similar to what has been observed in Bi-doped material in which the measured Hall coefficients support the transition from the hole to the electron conduction, albeit at much lower nominal dopant concentrations [61].

Furthermore, the bulk valence band, now fully occupied, displays a local minimum at the *L* point and two nearby maxima as it disperses along k_x [Figs. 4(h) and 4(i)]. Its dispersion is obtained from the peak position of the higher binding energy peaks in energy distribution curves, as represented by white points in Fig. 4(h).

So the question is why the In-doped $Pb_{1-x}Sn_xTe$ superconducting is only on the gap-inverted TCI side of the phase diagram [27]. After all, pure Pb has a higher T_c than Sn, and one could naively expect that the superconductivity will be stronger near $x = 0$. We think that the answer lies in the different shapes of the bands before and after the gap inversion, as presented in Fig. 5. On the trivial side, the valence and conduction bands have a single extremum along all three *k* axes (Fig. 1). On approaching the critical point at $x \approx 0.36$, these extrema approach each other and get lighter until they touch in a single (3D Dirac) point. On the topological side, far from the inversion point, the bands have a so-called Mexican hat band (MHB) shape [17,62–64]. Specifically, in the case of SnTe, both the valence and conducting bands have a single maximum (minimum) at the *L* point as they disperse along

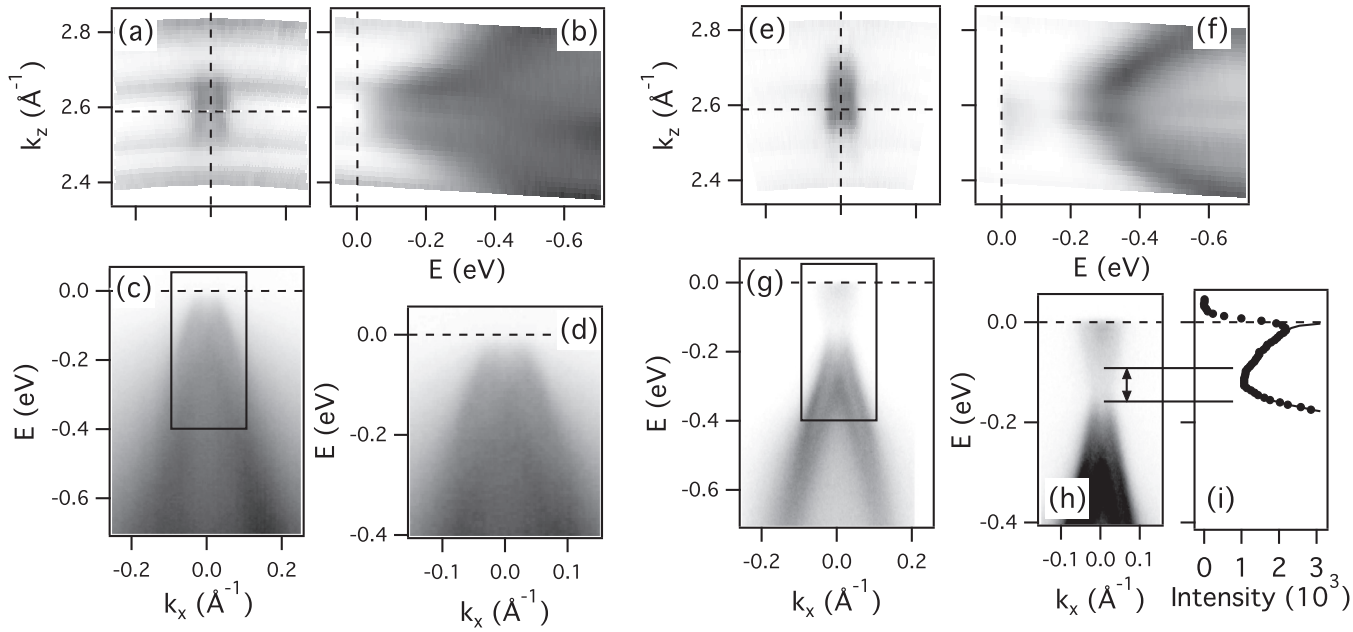

FIG. 3. Three-dimensional electronic structure of $Pb_{0.7}Sn_{0.3}Te$ and $(Pb_{0.7}Sn_{0.3})_{0.84}In_{0.16}Te$. (a) ARPES intensity at the Fermi level (Fermi surface) as a function of k_z along the Γ-L-Γ line of the BBZ and k_x along the $\bar{\Gamma}\bar{K}$ line of the SBZ for $Pb_{0.7}Sn_{0.3}Te$. (b) k_z dispersion of the valence band along the Γ-L-Γ line near the L point between the second and third BBZs. (c) Dispersion of the valence band along the $\bar{\Gamma}\bar{K}$ line of the SBZ, taken at 17 eV photon energy (corresponding to the W-L-W line of the bulk BZ). (d) Close-up of the spectral region marked by the rectangle in (c). (e)–(h) The corresponding plots for the In-doped sample, $(Pb_{0.7}Sn_{0.3})_{0.84}In_{0.16}Te$. The arrow in (h) represents the gap between the VB and CB, $\Delta_L \approx 65$ meV. (i) EDC at $k_x = 0$ from (h). The raw intensity and that divided by the Fermi distribution are plotted as dots and the solid line, respectively. The spectra in (a)–(d) and (e)–(i) were taken at 80 and 50 K, respectively.

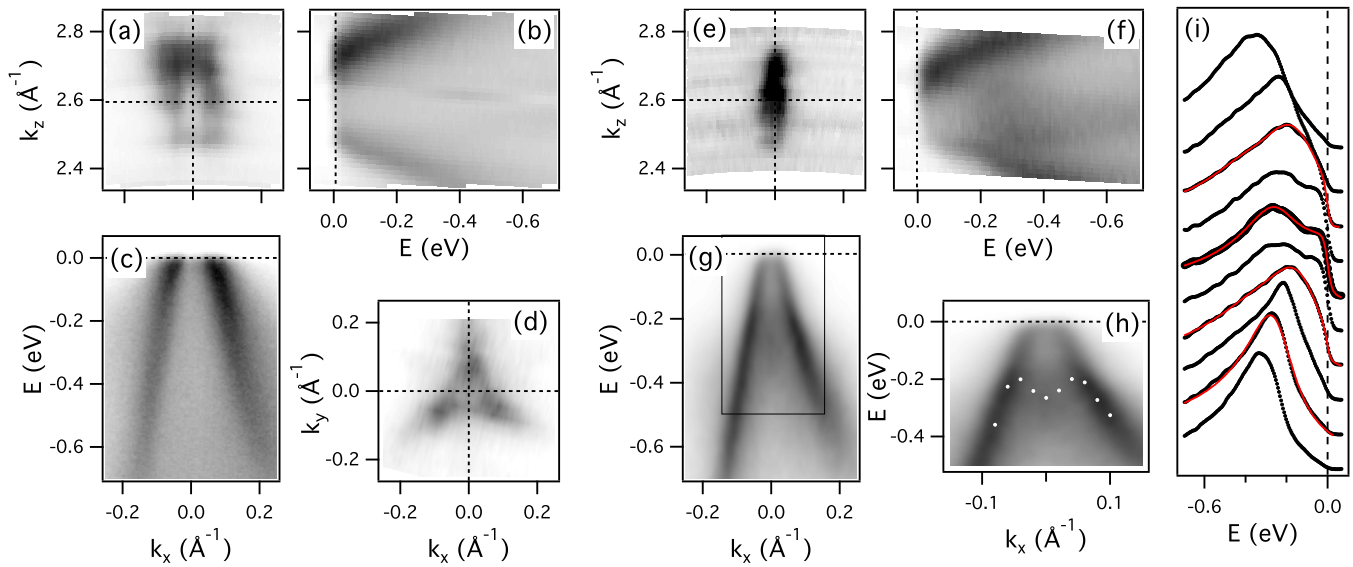

FIG. 4. Three-dimensional electronic structure of $Pb_{0.5}Sn_{0.5}Te$ and $(Pb_{0.5}Sn_{0.5})_{0.7}In_{0.3}Te$. (a) ARPES intensity at the Fermi level (Fermi surface) as a function of k_z along the Γ-L-Γ line of the BBZ and k_x along the $\bar{\Gamma}\bar{K}$ line of the SBZ for $Pb_{0.5}Sn_{0.5}Te$. (b) k_z dispersion of the valence band along the Γ-L-Γ line near the L point between the second and third BBZs. (c) Dispersion of the valence band along the $\bar{\Gamma}$-$\bar{K}$ line of the SBZ, taken at 17 eV photon energy (corresponding to the W-L-W line of the BBZ). (d) Constant-energy contour of in-plane ARPES intensity at $E = 0$ (Fermi surface) taken at $\hbar\nu = 17$ eV, corresponding to $k_z = 2.6$ Å. (e)–(g) The same as (a)–(c), but for the In-doped sample, $(Pb_{0.5}Sn_{0.5})_{0.7}In_{0.3}Te$. All the spectra were taken at 80 K. (h) Close-up of the spectral region marked by the rectangle in (g). The white points indicate dispersion (peak position) of the bulk valence band from fitting the EDCs in (i). (i) EDCs of the spectral intensities from (g) and (h) (black) with selected fitting curves (red). The thick spectrum corresponds to $k_x = 0$, or the L point in the bulk BZ.

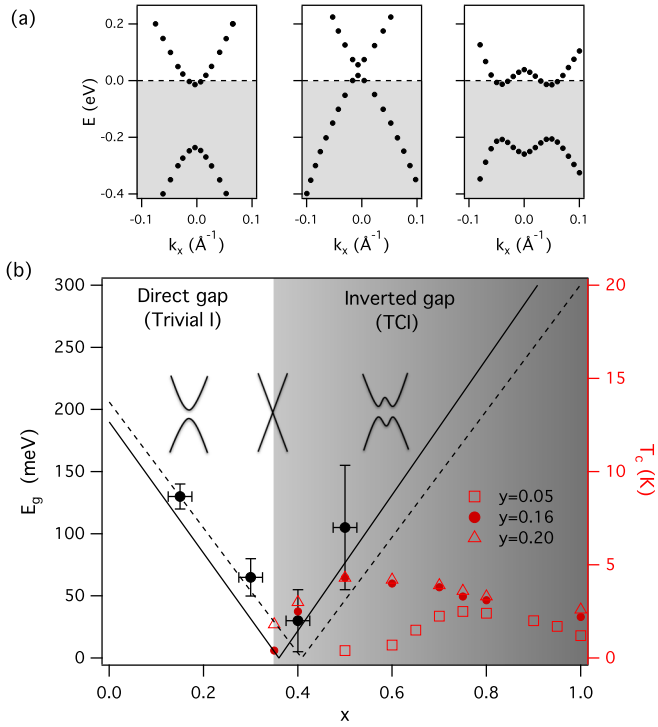

FIG. 5. Phase diagram of $(Pb_{1-x}Sn_x)_{1-y}In_yTe$. (a) Experimentally obtained in-plane dispersions of occupied (shaded) bulk states in $Pb_{0.85}Sn_{0.15}Te$ (left), $Pb_{0.6}Sn_{0.4}Te$ (middle), and $(Pb_{0.5}Sn_{0.5})_{0.7}In_{0.3}Te$ (right). The fitting of momentum distribution curves was performed for the first two cases, while EDC fitting was used in the third case. The unoccupied dispersions are inverted copies of the occupied ones. (b) The phase diagram of $(Pb_{1-x}Sn_x)_{1-y}In_yTe$. The solid (dashed) line represents the fundamental gap E_g at $T = 0$ ($T = 50$ K) in $Pb_{1-x}Sn_xTe$ from Heremans *et al.* [60]. The black circles are gap estimates from our measurements, as discussed in the text. Superconducting T_c data points for In-doped $Pb_{1-x}Sn_xTe$ (red symbols) are taken from Ref. [27].

the Γ-*L* line, whereas in the perpendicular direction or within the (111) plane, the bands are MHB, as realized early on by Tung and Cohen [62] and Rabii [65]. This is consistent with our experimental results [Figs. 4(e)–4(j)]. The density of states (DOS) near the tops (bottoms) of such a MHB can be dramatically enhanced relative to the band extrema on the trivial side, with the details depending on the models and dimensionality of the system [17,63,64]. Moreover, the transition from a 3D Dirac (linear) band to the MHB involves not only mass generation (gap opening) but also a flattening related to a transition from a single extremum to a MHB, which can further enhance the DOS and lead to singularities even in 3D systems [63]. We argue that this will necessarily have an augmenting effect on the properties of a material dependent on the DOS, as it will enhance electronic correlations, especially if the enhanced DOS can be brought near the chemical potential. In particular, we can expect that the electron-phonon coupling will be enhanced, eventually leading to superconductivity. The flat bands near the Fermi level are generally unstable against other symmetry breaking phases, such as charge density waves and magnetism, but in In-doped $Pb_{1-x}Sn_xTe$, the superconductivity is the ground state tied to the MHB. Moreover, since the MHBs are inverted, the materials that possess them are excellent candidates for intrinsic topological superconductors.

We note that both the gap magnitudes and the details of the dispersions in the valence and conduction bands shown in Fig. 5 depend on the analysis. They also depend on temperature in both theoretical and experimental studies. Our clearest cases are $Pb_{0.85}Sn_{0.15}Te$ and $(Pb_{0.7}Sn_{0.3})_{0.84}In_{0.16}Te$, in which both valence and conduction bands are visible, suggesting that the most appropriate method for gap determination is by the steep onsets of emission at band extrema [Figs. 1(e), 1(f), 3(h), and 3(i)]. For the remaining samples, the gap determination is less reliable. For example, in $Pb_{0.6}Sn_{0.4}Te$, the room temperature measurements displayed no detectable gap, and we set the value of ∼30 meV as the upper limit for a low-temperature gap. In the pure $Pb_{0.3}Sn_{0.7}Te$ sample, the conduction band is clearly out of reach of ARPES [Figs. 3(c) and 3(d)]. However, we were able to detect its threshold at room temperature after depositing potassium on the surface. The extracted gap was ∼150 meV, much larger than the one seen in the In-doped sample at low temperature, but when adjusted for temperature using the known thermal coefficients, the gaps were almost identical (∼65 meV at 50 K). Also, the room temperature spectrum of the $Pb_{0.4}Sn_{0.6}Te$ sample shows essentially no gap, but we have set 30 meV as an upper limit at low temperature. In the $(Pb_{0.5}Sn_{0.5})_{0.7}In_{0.3}Te$ case, the gap is determined from the dispersion of the peak maximum of the valence band and the assumption that the chemical potential is near the bottom of the conduction band [Figs. 4(h) and 4(i)]. From the $Pb_{0.85}Sn_{0.15}Te$ case, we know that the distance between the sharp onset of emission and the peak maximum can be quite significant (∼50 meV), which would lead to a large overestimate for the gaps determined from peak positions. Therefore, in Fig. 5, we have adjusted the gap magnitudes obtained from peak dispersions to those that would correspond to the onset of emission for both $x = 0.15$ and $x = 0.5$. Also, there is some ambiguity in how the gap is actually defined in the inverted case, where the bands display the MHB dispersion. However, the most important finding of our study, that the In-doped $Pb_{1-x}Sn_xTe$ displays the MHB dispersion on the TCI side of the phase diagram, where superconductivity occurs, does not depend on those details.

On the other hand, the question of whether the superconductivity in $(Pb_{1-x}Sn_x)_{1-y}In_yTe$ is conventional or topological is still open. Topological superconductors are accompanied by gapless states at their boundaries, and they may be composed of Majorana fermions. Point-contact spectroscopy of In-doped SnTe suggests odd-parity pairing and topological superconductivity [42], but the specific heat reveals a fully gapped superconductivity that would argue against it [66]. Similarly, the STM measurements of the superconducting gap in $(Pb_{0.5}Sn_{0.5})_{0.7}In_{0.3}Te$ on the (001) surface suggest that the sample seems to be fully gapped, without in-gap states—contrary to what would be expected for a topological superconductor [67]. However, we note that those measurements were performed on (100) surfaces of bulk crystals that poorly cleave. In addition, topological surface states on the (100) surfaces are different from those on the (111) surfaces studied here, and their ability to support the zero modes might also be different [16]. Therefore, it would be highly desirable

to perform scanning tunneling microscopy studies of the (111) surfaces. Our ARPES results unambiguously show that the superconductivity in In-doped $Pb_{1-x}Sn_xTe$ occurs not only on the topological side of the phase diagram but also because of its topological character, with the inverted MHBs playing the decisive role. Therefore, In-doped $Pb_{1-x}Sn_xTe$ is a TCI (for $x \geqslant 0.36$) and is also a superconductor, but it remains to be seen whether it is a topological superconductor with an odd order parameter and in-gap states. We hope that our results will stimulate further studies capable of answering these questions directly.

ACKNOWLEDGMENTS

This work was supported by the U.S. Department of Energy, Office of Basic Energy Sciences, Contract No. DE-SC0012704, and the ARO MURI program, Grant No. W911NF-12-1-0461.

[1] S. Murakami, Phase transition between the quantum spin Hall and insulator phases in 3D: Emergence of a topological gapless phase, New J. Phys. **9**, 356 (2007).

[2] S. Murakami, S. Iso, Y. Avishai, M. Onoda, and N. Nagaosa, Tuning phase transition between quantum spin Hall and ordinary insulating phases, Phys. Rev. B **76**, 205304 (2007).

[3] B.-J. Yang and N. Nagaosa, Classification of stable three-dimensional Dirac semimetals with nontrivial topology, Nat. Commun. **5**, 4898 (2014).

[4] B. A. Volkov and O. A. Pankratov, Two-dimensional massless electrons in an inverted contact, JETP Lett. **42**, 178 (1985).

[5] E. Fradkin, E. Dagotto, and D. Boyanovsky, Physical realization of the parity anomaly in condensed matter physics, Phys. Rev. Lett. **57**, 2967 (1986).

[6] S. Murakami, N. Nagaosa, and S.-C. Zhang, Spin-Hall insulator, Phys. Rev. Lett. **93**, 156804 (2004).

[7] C. L. Kane and E. J. Mele, Z_2 topological order and the quantum spin Hall effect, Phys. Rev. Lett. **95**, 146802 (2005).

[8] B. A. Bernevig, T. L. Hughes, and S.-C. Zhang, Quantum spin Hall effect and topological phase transition in HgTe quantum wells, Science **314**, 1757 (2006).

[9] M. Konig, S. Wiedmann, C. Brune, A. Roth, H. Buhmann, L. W. Molenkamp, X. L. Qi, and S. C. Zhang, Quantum spin Hall insulator state in HgTe quantum wells, Science **318**, 766 (2007).

[10] L. Fu, C. L. Kane, and E. J. Mele, Topological insulators in three dimensions, Phys. Rev. Lett. **98**, 106803 (2007).

[11] H.-J. Noh, H. Koh, S.-J. Oh, J.-H. Park, H.-D. Kim, J. D. Rameau, T. Valla, T. E. Kidd, P. D. Johnson, Y. Hu, and Q. Li, Spin-orbit interaction effect in the electronic structure of Bi_2Te_3 observed by angle-resolved photoemission spectroscopy, Europhys. Lett. **81**, 57006 (2008).

[12] M. König, H. Buhmann, L. W. Molenkamp, T. Hughes, C.-X. Liu, X.-L. Qi, and S.-C. Zhang, The quantum spin Hall effect: Theory and experiment, J. Phys. Soc. Jpn. **77**, 031007 (2008).

[13] D. Hsieh, D. Qian, L. Wray, Y. Xia, Y. S. Hor, R. J. Cava, and M. Z. Hasan, A topological Dirac insulator in a quantum spin Hall phase, Nature (London) **452**, 970 (2008).

[14] L. Fu, Topological crystalline insulators, Phys. Rev. Lett. **106**, 106802 (2011).

[15] S.-Y. Xu *et al.*, Observation of a topological crystalline insulator phase and topological phase transition in $Pb_{1-x}Sn_xTe$, Nat. Commun. **3**, 1192 (2012).

[16] J. Liu, W. Duan, and L. Fu, Two types of surface states in topological crystalline insulators, Phys. Rev. B **88**, 241303(R) (2013).

[17] G. Yang, J. Liu, L. Fu, W. Duan, and C. Liu, Weak topological insulators in PbTe/SnTe superlattices, Phys. Rev. B **89**, 085312 (2014).

[18] I. Pletikosić, G. D. Gu, and T. Valla, Inducing a Lifshitz transition by extrinsic doping of surface bands in the topological crystalline insulator $Pb_{1-x}Sn_xSe$, Phys. Rev. Lett. **112**, 146403 (2014).

[19] A. Gyenis, I. K. Drozdov, S. Nadj-Perge, O. B. Jeong, J. Seo, I. Pletikosić, T. Valla, G. D. Gu, and A. Yazdani, Quasiparticle interference on the surface of the topological crystalline insulator $Pb_{1-x}Sn_xSe$, Phys. Rev. B **88**, 125414 (2013).

[20] A. Svane, N. E. Christensen, M. Cardona, A. N. Chantis, M. van Schilfgaarde, and T. Kotani, Quasiparticle self-consistent GW calculations for PbS, PbSe, and PbTe: Band structure and pressure coefficients, Phys. Rev. B **81**, 245120 (2010).

[21] S. Suchalkin, M. Ermolaev, T. Valla, G. Kipshidze, D. Smirnov, S. Moon, M. Ozerov, Z. Jiang, Y. Jiang, S. P. Svensson, W. L. Sarney, and G. Belenky, Dirac energy spectrum and inverted bandgap in metamorphic InAsSb/InSb superlattices, Appl. Phys. Lett. **116**, 032101 (2020).

[22] Z. Wang, Y. Sun, X.-Q. Chen, C. Franchini, G. Xu, H. Weng, X. Dai, and Z. Fang, Dirac semimetal and topological phase transitions in A_3Bi (A = Na, K, Rb), Phys. Rev. B **85**, 195320 (2012).

[23] Z. Wang, H. Weng, Q. Wu, X. Dai, and Z. Fang, Three-dimensional Dirac semimetal and quantum transport in Cd_3As_2, Phys. Rev. B **88**, 125427 (2013).

[24] Z. K. Liu, B. Zhou, Y. Zhang, Z. J. Wang, H. M. Weng, D. Prabhakaran, S.-K. Mo, Z. X. Shen, Z. Fang, X. Dai, Z. Hussain, and Y. L. Chen, Discovery of a three-dimensional topological Dirac semimetal, Na_3Bi, Science **343**, 864 (2014).

[25] S. Borisenko, Q. Gibson, D. Evtushinsky, V. Zabolotnyy, B. Büchner, and R. J. Cava, Experimental realization of a three-dimensional dirac semimetal, Phys. Rev. Lett. **113**, 027603 (2014).

[26] M. Neupane, S.-Y. Xu, R. Sankar, N. Alidoust, G. Bian, C. Liu, I. Belopolski, T.-R. Chang, H.-T. Jeng, H. Lin, A. Bansil, F. Chou, and M. Z. Hasan, Observation of a three-dimensional topological Dirac semimetal phase in high-mobility Cd_3As_2, Nat. Commun. **5**, 3786 (2014).

[27] G. Bushmarina, I. Drabkin, D. Mashovets, R. Parfeniev, D. Shamshur, and M. Shachov, Superconducting properties of the SnTe-PbTe system doped with indium, Phys. B (Amsterdam, Neth.) **169**, 687 (1991).

[28] V. I. Kozub, R. V. Parfen'ev, D. V. Shamshur, D. V. Shakura, A. V. Chernyaev, and S. A. Nemov, Superconductor-insulator transition in $(Pb_zSn_{1-z})_{0.84}In_{0.16}Te$, JETP Lett. **84**, 35 (2006).

[29] R. D. Zhong, J. A. Schneeloch, T. S. Liu, F. E. Camino, J. M. Tranquada, and G. D. Gu, Superconductivity induced by In substitution into the topological crystalline insulator $Pb_{0.5}Sn_{0.5}Te$, Phys. Rev. B **90**, 020505(R) (2014).

[30] R. Zhong, X. He, J. A. Schneeloch, C. Zhang, T. Liu, I. Pletikosić, T. Yilmaz, B. Sinkovic, Q. Li, W. Ku, T. Valla, J. M. Tranquada, and G. Gu, Surface-state-dominated transport in crystals of the topological crystalline insulator In-doped $Pb_{1-x}Sn_xTe$, Phys. Rev. B **91**, 195321 (2015).

[31] R. Zhong, J. Schneeloch, Q. Li, W. Ku, J. Tranquada, and G. Gu, Indium substitution effect on the topological crystalline insulator family $(Pb_{1-x}Sn_x)_{1-y}In_yTe$: topological and superconducting properties, Crystals **7**, 55 (2017).

[32] A. Sapkota, Y. Li, B. L. Winn, A. Podlesnyak, G. Xu, Z. Xu, K. Ran, T. Chen, J. Sun, J. Wen, L. Wu, J. Yang, Q. Li, G. D. Gu, and J. M. Tranquada, Electron-phonon coupling and superconductivity in the doped topological crystalline insulator $(Pb_{0.5}Sn_{0.5})_{1-x}In_xTe$, Phys. Rev. B **102**, 104511 (2020).

[33] Y. H. Lin, J. Nelson, and A. M. Goldman, Superconductivity of very thin films: The superconductor–insulator transition, Phys. C (Amsterdam, Neth.) **514**, 130 (2015).

[34] A. L. Chudnovskiy and A. Kamenev, Superconductor-insulator transition in a non-Fermi liquid, Phys. Rev. Lett. **129**, 266601 (2022).

[35] L. Fu and C. L. Kane, Superconducting proximity effect and Majorana fermions at the surface of a topological insulator, Phys. Rev. Lett. **100**, 096407 (2008).

[36] T. M. Rice and M. Sigrist, Sr_2RuO_4: An electronic analogue of ^{3}He? J. Phys.: Condens. Matter **7**, L643 (1995).

[37] K. Ishida, H. Mukuda, Y. Kitaoka, K. Asayama, Z. Q. Mao, Y. Mori, and Y. Maeno, Spin-triplet superconductivity in Sr_2RuO_4 identified by ^{17}O Knight shift, Nature (London) **396**, 658 (1998).

[38] S. Das Sarma, C. Nayak, and S. Tewari, Proposal to stabilize and detect half-quantum vortices in strontium ruthenate thin films: Non-Abelian braiding statistics of vortices in a $p_x + ip_y$ superconductor, Phys. Rev. B **73**, 220502(R) (2006).

[39] A. Pustogow, Y. Luo, A. Chronister, Y.-S. Su, D. A. Sokolov, F. Jerzembeck, A. P. Mackenzie, C. W. Hicks, N. Kikugawa, S. Raghu, E. D. Bauer, and S. E. Brown, Constraints on the superconducting order parameter in Sr_2RuO_4 from oxygen-17 nuclear magnetic resonance, Nature (London) **574**, 72 (2019).

[40] Y. S. Hor, A. J. Williams, J. G. Checkelsky, P. Roushan, J. Seo, Q. Xu, H. W. Zandbergen, A. Yazdani, N. P. Ong, and R. J. Cava, Superconductivity in $Cu_xBi_2Se_3$ and its implications for pairing in the undoped topological insulator, Phys. Rev. Lett. **104**, 057001 (2010).

[41] A. S. Erickson, J.-H. Chu, M. F. Toney, T. H. Geballe, and I. R. Fisher, Enhanced superconducting pairing interaction in indium-doped tin telluride, Phys. Rev. B **79**, 024520 (2009).

[42] S. Sasaki, Z. Ren, A. A. Taskin, K. Segawa, L. Fu, and Y. Ando, Odd-parity pairing and topological superconductivity in a strongly spin-orbit coupled semiconductor, Phys. Rev. Lett. **109**, 217004 (2012).

[43] S. Sasaki, K. Segawa, and Y. Ando, Superconductor derived from a topological insulator heterostructure, Phys. Rev. B **90**, 220504(R) (2014).

[44] H. Luo, K. Yan, I. Pletikosic, W. Xie, B. F. Phelan, T. Valla, and R. J. Cava, Superconductivity in a misfit phase that combines the topological crystalline insulator $Pb_{1-x}Sn_xSe$ with the CDW-bearing transition metal dichalcogenide $TiSe_2$, J. Phys. Soc. Jpn. **85**, 064705 (2016).

[45] M.-X. Wang, C. Liu, J.-P. Xu, F. Yang, L. Miao, M.-Y. Yao, C. L. Gao, C. Shen, X. Ma, X. Chen, Z.-A. Xu, Y. Liu, S.-C. Zhang, D. Qian, J.-F. Jia, and Q.-K. Xue, The coexistence of superconductivity and topological order in the Bi_2Se_3 thin films, Science **336**, 52 (2012).

[46] H. Yi, L.-H. Hu, Y. Wang, R. Xiao, J. Cai, D. R. Hickey, C. Dong, Y.-F. Zhao, L.-J. Zhou, R. Zhang, A. R. Richardella, N. Alem, J. A. Robinson, M. H. W. Chan, X. Xu, N. Samarth, C.-X. Liu, and C.-Z. Chang, Crossover from Ising- to Rashba-type superconductivity in epitaxial Bi_2Se_3/monolayer $NbSe_2$ heterostructures, Nat. Mater. **21**, 1366 (2022).

[47] P. Zareapour, A. Hayat, S. Y. F. Zhao, M. Kreshchuk, A. Jain, D. C. Kwok, N. Lee, S.-W. Cheong, Z. Xu, A. Yang, G. D. Gu, S. Jia, R. J. Cava, and K. S. Burch, Proximity-induced high-temperature superconductivity in the topological insulators Bi_2Se_3 and Bi_2Te_3, Nat. Commun. **3**, 1056 (2012).

[48] E. Wang, H. Ding, A. V. Fedorov, W. Yao, Z. Li, Y.-F. Lv, K. Zhao, L.-G. Zhang, Z. Xu, J. Schneeloch, R. Zhong, S.-H. Ji, L. Wang, K. He, X. Ma, G. Gu, H. Yao, Q.-K. Xue, X. Chen, and S. Zhou, Fully gapped topological surface states in Bi_2Se_3 films induced by a d-wave high-temperature superconductor, Nat. Phys. **9**, 621 (2013).

[49] T. Yilmaz, I. Pletikosić, A. P. Weber, J. T. Sadowski, G. D. Gu, A. N. Caruso, B. Sinkovic, and T. Valla, Absence of a proximity effect for a thin-films of a Bi_2Se_3 topological insulator grown on top of a $Bi_2Sr_2CaCu_2O_{8+\delta}$ cuprate superconductor, Phys. Rev. Lett. **113**, 067003 (2014).

[50] A. K. Kundu, Z. Wu, I. Drozdov, G. Gu, and T. Valla, Origin of suppression of proximity-induced superconductivity in $Bi/Bi_2Sr_2CaCu_2O_{8+\delta}$ heterostructures, Adv. Quantum Technol. **3**, 2000038 (2020).

[51] A. K. Kundu, G. Gu, and T. Valla, Quantum size effects, multiple Dirac cones, and edge states in ultrathin Bi(110) films, ACS Appl. Mater. Interfaces **13**, 33627 (2021).

[52] C. K. Kim, I. K. Drozdov, K. Fujita, J. C. S. Davis, I. Božović, and T. Valla, In-situ angle-resolved photoemission spectroscopy of copper-oxide thin films synthesized by molecular beam epitaxy, J. Electron Spectrosc. Relat. Phenom. **257**, 146775 (2022).

[53] A. Strauss, Inversion of conduction and valence bands in $Pb_{1-x}Sn_xSe$ alloys, Phys. Rev. **157**, 608 (1967).

[54] S. Ran, C. Eckberg, Q. P. Ding, Y. Furukawa, T. Metz, S. R. Saha, I. L. Liu, M. Zic, H. Kim, J. Paglione, and N. P. Butch, Nearly ferromagnetic spin-triplet superconductivity, Science **365**, 684 (2019).

[55] Y. Yu, V. Madhavan, and S. Raghu, Majorana fermion arcs and the local density of states of UTe_2, Phys. Rev. B **105**, 174520 (2022).

[56] C. M. Polley, P. Dziawa, A. Reszka, A. Szczerbakow, R. Minikayev, J. Z. Domagala, S. Safaei, P. Kacman, R. Buczko, J. Adell, M. H. Berntsen, B. M. Wojek, O. Tjernberg, B. J. Kowalski, T. Story, and T. Balasubramanian, Observation of topological crystalline insulator surface states on (111)-oriented $Pb_{1-x}Sn_xSe$ films, Phys. Rev. B **89**, 075317 (2014).

[57] J. Dimmock, I. Melngailis, and A. Strauss, Band structure and laser action in $Pb_xSn_{1-x}Te$, Phys. Rev. Lett. **16**, 1193 (1966).

[58] S. Takaoka, S. Shimomura, H. Takahashi, and K. Murase, Band-edge structure of indium-doped $Pb_{1-x}Sn_xTe$ across the band-inversion region investigated by the far-infrared magnetoplasma method, Phys. Rev. B **40**, 5642 (1989).

[59] B. Turowski, A. Kazakov, R. Rudniewski, T. Sobol, E. Partyka-Jankowska, T. Wojciechowski, M. Aleszkiewicz, W. Zaleszczyk, M. Szczepanik, T. Wojtowicz, and V. V. Volobuev, Spin-polarization of topological crystalline and normal insulator $Pb_{1-x}Sn_xSe$ (111) epilayers probed by photoelectron spectroscopy, Appl. Surf. Sci. **610**, 155434 (2023).

[60] J. P. Heremans, B. Wiendlocha, and A. M. Chamoire, Resonant levels in bulk thermoelectric semiconductors, Energy Environ. Sci. **5**, 5510 (2012).

[61] V. V. Volobuev, P. S. Mandal, M. Galicka, O. Caha, J. Sánchez-Barriga, D. Di Sante, A. Varykhalov, A. Khiar, S. Picozzi, G. Bauer, P. Kacman, R. Buczko, O. Rader, and G. Springholz, Giant Rashba splitting in $Pb_{1-x}Sn_xTe$ (111) topological crystalline insulator films controlled by Bi doping in the bulk, Adv. Mater. **29**, 1604185 (2017).

[62] Y. W. Tung and M. L. Cohen, The fundamental energy gap in SnTe and PbTe, Phys. Lett. A **29**, 236 (1969).

[63] X.-G. He, X. Xi, and W. Ku, Generic symmetry breaking instability of topological insulators due to a novel van Hove singularity, arXiv:1410.2885.

[64] H. Xu, J. Zhou, H. Wang, and J. Li, Giant photonic response of Mexican-hat topological semiconductors for mid-infrared to terahertz applications, J. Phys. Chem. Lett. **11**, 6119 (2020).

[65] S. Rabii, Energy-band structure and electronic properties of SnTe, Phys. Rev. **182**, 821 (1969).

[66] M. Novak, S. Sasaki, M. Kriener, K. Segawa, and Y. Ando, Unusual nature of fully gapped superconductivity in In-doped SnTe, Phys. Rev. B **88**, 140502(R) (2013).

[67] G. Du, Z. Du, D. Fang, H. Yang, R. D. Zhong, J. Schneeloch, G. D. Gu, and H.-H. Wen, Fully gapped superconductivity in In-doped topological crystalline insulator $Pb_{0.5}Sn_{0.5}Te$, Phys. Rev. B **92**, 020512(R) (2015).